

Persistent Homology and Many-Body Atomic Structure for Medium-Range Order in the Glass

Takenobu Nakamura¹, Yasuaki Hiraoka², Akihiko Hirata¹,
Emerson G. Escobar³ and Yasumasa Nishiura¹

E-mail: t.nakamura@wpi-aimr.tohoku.ac.jp

¹ WPI-AIMR, Tohoku University, Japan

² Institute of Mathematics for Industry, Kyushu University, Japan

³ Graduate School of Mathematics, Kyushu University, Japan

Abstract. Characterization of medium-range order in amorphous materials and its relation to short-range order is discussed. A new topological approach is presented here to extract a hierarchical structure of amorphous materials, which is robust against small perturbations and allows us to distinguish it from periodic or random configurations. The method is called the persistence diagram (PD) and it introduces scales into many-body atomic structures in order to characterize the size and shape. We first illustrate how perfect crystalline and random structures are represented in the PDs. Then, the medium-range order in the amorphous silica is characterized by using the PD. The PD approach reduces the size of the data tremendously to much smaller geometrical summaries and has a huge potential to be applied to broader areas including complex molecular liquid, granular materials, and metallic glasses.

PACS numbers: 61.43.Er, 61.43.Fs, 02.40.Re

1. Introduction

Glasses have become increasingly useful and popular in materials engineering and industry. Nevertheless, its microscopic structure is not as clearly understood as crystalline solids. This is mainly due to the lack of long-range order (LRO). Hence the local structures, instead of LRO, have been extensively studied to characterize amorphous structures. In particular, short-range order (SRO), which describes atomic configurations of nearest neighbors, was well understood both experimentally and theoretically. However, it becomes clear that the larger-scale structures beyond neighbor atoms so-called medium-range order (MRO) are much more important than SRO in glasses. The amorphous structures are essentially characterized by possible connection of SRO that can build up continuous atomic configurations throughout the materials without any periodicity [1, 2, 3, 4, 5, 6, 7, 8].

The intrinsic structural features of MRO can be detected in several ways. For example, the split of the second peak in the radial distribution function is a sign for amorphous metals, whereas the first sharp diffraction peak of the structure factor is a sign for covalent amorphous solids [8]. Although these signs are evidence for the existence of MRO, their geometric origins are not clearly understood like the “periodicity” of LRO or the “chemical or packing order” of SRO. This is because MRO is definitely generated by many-body configurations, and the 2-body distributions such as the radial distribution or the structure factor does not properly describe its geometry.

To describe the many-body atomic structure appearing in amorphous solids, angle distributions and statistics of topological quantities have been widely used so far. The bond-angle and torsion-angle distributions extract the partial information of 3-body and 4-body configurations, respectively [1]. Even though these variables describe the configurations beyond the nearest neighbor, the scope of the scale is restricted within $m(\leq 4)$ -body configurations.

On the other hand, the topological quantification of amorphous structures such as the ring statistics and the Voronoi polyhedral analyses have been used to characterize atomic configurations of covalent and metallic amorphous solids, respectively. [1, 2, 9, 10, 11, 12, 13, 14, 15, 16, 17]. These methods do not restrict the number of atoms to be considered, and are useful to classify the variety of many-body atomic structure in certain situations. However, they require building some geometric models from atomic configurations based on artificial criteria such as a threshold of the bond length. Furthermore, they do not explicitly extract the length scale. Hence they are not suitable for studying multi-scale phenomena, which are supposed to be important to determine MRO. Systematic methodologies to study many-body atomic structure with metric information are highly desired.

In recent years, persistent homology and its graphical representation, called the persistence diagram (PD), have been invented in the applied mathematics community as a systematic method to extract geometric properties embedded in point cloud data [18, 19]. By regarding the atomic configuration as a point cloud data, we can apply

the method for geometric analysis of materials. Significantly, this method can deal with many-body configurations, and also can provide two length-scales, *birth* and *death scales*, which characterize the size of the n -dimensional holes. Namely, topological properties with metric information can be derived. Furthermore, PDs can be computed quite efficiently [20, 21, 22] so that it can handle complex configurations with a huge amount of atoms obtained by molecular dynamics (MD) simulations. Based on these observations, the PD approach is expected to be an adequate tool to characterize MRO in a systematic way.

In this paper, we propose a methodology based on PDs to characterize MRO in amorphous solids. We first provide a brief introduction of PDs mainly for readers not familiar with them. Then we show two examples to illustrate the geometric meaning of PDs by using FCC crystal and a uniform random configuration. Then, we calculated PDs for the atomic configurations of amorphous silica obtained by MD simulations. Our method can be applied to a wide class of amorphous solids and complex liquids with atomic configuration data. Here, we chose amorphous silica, since it is one of the standard amorphous solids, and hence, is an appropriate model material for comparing our method to the other conventional tools such as ring statistics. Moreover, the extensivity of the Betti numbers, the structural hierarchy of the geometric objects appearing in PDs, and the decomposition method into single atomic components are also explained. From these arguments, we elucidate the geometry of MRO in amorphous silica. As a consequence, we conclude that the PD analysis is an appropriate method to describe MRO, complementary to the existing tools.

2. Persistence Diagram

The input for computing persistence diagrams is a pair $\mathcal{A} = (Q, R)$ of an atomic configuration $Q = (\vec{x}_1, \vec{x}_2, \dots, \vec{x}_N)$ and radius parameters $R = (r_1, r_2, \dots, r_N)$ for an N -atom system. Here, $\vec{x}_i \in \mathbb{R}^3$ and r_i are the three-dimensional position and the input radius of the i -th atom, respectively. Instead of setting a threshold by an artificial criterion and giving bonds between atoms, we introduce a ball $B_i(\alpha) = \{\vec{x} \in \mathbb{R}^3 \mid \|\vec{x} - \vec{x}_i\| \leq r_i(\alpha)\}$ at \vec{x}_i with radius $r_i(\alpha) = \sqrt{\alpha + r_i^2}$ for each i -th atom parameterized by α . Then, we study persistent topological features in the union of balls $B(\alpha) = \bigcup_{i=1}^N B_i(\alpha)$ by changing the variable α . Typically, for a increasing family of α , this is a set of inflating atomic balls with centered at \vec{x}_i .

For each α , n -dimensional holes in $B(\alpha)$ such as clusters, rings, and cavities for $n = 0, 1$, and 2 , respectively, can be identified by homology [23]. Then, for each n -dimensional hole c_k , we can uniquely assign values $\alpha = b_k$ and $\alpha = d_k$ at which c_k first appears and disappears, respectively. These values b_k and d_k are called the birth and death scales of the hole c_k . The collection

$$D_n(\mathcal{A}) \equiv \{(b_k, d_k) \in \mathbb{R}^2 \mid k = 1, 2, \dots\} \quad (1)$$

of all these birth and death scales (b_k, d_k) is called the n -dimensional persistence diagram of \mathcal{A} . Here, we remark that the minimum value α_{\min} of α can be negative, i.e.,

$\alpha_{\min} = -\min\{r_1^2, r_2^2, \dots, r_N^2\}$, and the dimension of α (therefore b_k and d_k) is length squared.

The PD is a two-dimensional scatter plot. It follows from $b_k < d_k$ that the points in the PD appear above the diagonal. From the construction, the birth and death points (b_k, d_k) are determined by the m -body atomic configuration $\vec{x}_{i_1}, \vec{x}_{i_2}, \dots, \vec{x}_{i_m}$ comprising of the k -th hole c_k . Namely, the birth and death scales are represented by $b_k = b_k(\vec{x}_{i_1}, \vec{x}_{i_2}, \dots, \vec{x}_{i_m})$ and $d_k = d_k(\vec{x}_{i_1}, \vec{x}_{i_2}, \dots, \vec{x}_{i_m})$. Different from the existing many-body variables such as bond angle $\theta_k = \theta_k(\vec{x}_{i_1}, \vec{x}_{i_2}, \vec{x}_{i_3})$ represented by $m = 3$, or torsion angle $\phi_k = \phi_k(\vec{x}_{i_1}, \vec{x}_{i_2}, \vec{x}_{i_3}, \vec{x}_{i_4})$ represented by $m = 4$, the number m of atoms to be considered is not restricted for the birth and death scales. Therefore b_k and d_k are reduced variables of metric properties of c_k . We use these variables to describe MRO.

Intuitively, the birth scale b_k indicates the maximum neighboring distance in $\vec{x}_{i_1}, \vec{x}_{i_2}, \dots, \vec{x}_{i_m}$, because c_k appears when the largest bond ($n = 1$) or cap ($n = 2$) in c_k is created. On the other hand, the death scale d_k indicates the size of c_k , because c_k disappears when it is covered up in the inflated atomic ball model $\bigcup_{i=1}^N B_i(\alpha)$.

We also introduce the life scale $d_k - b_k$ that represents the robustness of the hole c_k under the change of the variable α . Then, the points far from the diagonal in the PD have long life scales, meaning that they persist in a wide range of α . In contrast, the points close to the diagonal, i.e., small life scales, correspond to holes that are sensitive to α and can be considered noise.

In terms of the characterization of MRO, the life and death scales are important. The former distinguishes the proper geometric objects from the topological noise, whereas the latter represents the sizes of holes.

Persistent diagrams can be computed efficiently using freely available open-source software [20, 21]. For the geometric model of the union of balls structure, we use the alpha shapes module in CGAL [22]. We remark that even though the molecular simulations for bulk systems use periodic boundary conditions, we work with the point cloud data as a set of points in \mathbb{R}^3 as input to the PDs. Hence, some differences will appear when we count the holes across the boundary, although these effects are negligible in a sufficiently large system.

3. Typical Examples

Before analyzing the covalent glass structure, we introduce two typical examples. For simplicity, we only consider monatomic systems. For a monatomic system, the input to the PDs is given by the configuration of its atoms and a uniform input radius r for all the atoms. By the construction of $D_n(\mathcal{A})$, PDs calculated with a given radius r are the same as ones with $r = 0$ after the transformation $(b_k, d_k) \rightarrow (b_k + r^2, d_k + r^2)$. Hence, we choose the input radius to be zero, and hence the radius with the scale α is given by $r(\alpha) = \sqrt{\alpha}$.

The first example is a periodic configuration as a model of perfect crystal. In particular, we choose the FCC crystal. In the unit cell, there are 4 atomic sites at

$(0, 0, 0)$, $(1/\sqrt{2}, 1/\sqrt{2}, 0)$, $(1/\sqrt{2}, 0, 1/\sqrt{2})$ and $(0, 1/\sqrt{2}, 1/\sqrt{2})$ and the three primitive lattice vectors are set to be $(\sqrt{2}, 0, 0)$, $(0, \sqrt{2}, 0)$ and $(0, 0, \sqrt{2})$. Therefore the number density is $\rho = \sqrt{2}$. These lengths are chosen to make the distance between nearest neighbors unity. We prepare a cubic cluster of the FCC crystal in such a way that the number of unit cells along each edge is n_L , the length of each side is $L = \sqrt{2}n_L$, and hence, the number of atoms is $N = 4n_L^3$.

The top panels in Fig. 1 show the PDs for the FCC. Because of the periodicity, only a few points, each with high multiplicity, are found in each PD. The point at $(0, 1/4)$ in D_0 represents the length to contact the nearest neighbor. This is because each inflated atomic ball contacts its nearest neighbor atoms at $r_i(\alpha) = 1/2$, i.e., $\alpha = 1/4$. In the same way, the point at $(1/4, 1/3)$ in D_1 represents equilateral triangle rings, and the points $(1/3, 3/8)$ and $(1/3, 1/2)$ in D_2 represent regular tetrahedral and octahedral cavities, respectively. Here, the open circles at the points close to $(1/2, 1/2)$ in D_1 and D_2 represent rings that are regular squares or isosceles right triangles and cavities of isosceles right triangular pyramids, respectively. These holes are parts of a perfect octahedron. As the radius of atomic ball becomes large, these holes are instantly covered right after they appeared.

The periodicity also leads to high multiplicity. By a simple geometric consideration, the multiplicities at $(0, 1/4)$ in D_0 , $(1/4, 1/3)$ in D_1 , and $(1/3, 3/8)$ and $(1/3, 1/2)$ in D_2 are calculated as $m_{\text{N.Neighb}} = 4n_L^3 - 1$, $m_{\text{Tri.}} = 20n_L^3 - 24n_L^2 + 6n_L + 1$, $m_{\text{Tetra.}} = (2n_L - 1)^3$ and $m_{\text{Octa.}} = 4(n_L - 1)^3$ respectively. The coefficients of n_L^3 represent how many clusters, rings, and cavities exist in the unit cell in the bulk system. Specifically, in the unit cell, there are 4 particles, 8 tetrahedra and 4 octahedra. Every ring in the unit cell is a regular triangle, and is shared by a tetrahedron and an octahedron. Therefore we only need to count the number of rings in the octahedra. Each octahedron has 8 triangles on the surface, and thus there are 32 triangle rings in the unit cell. However, in each octahedron, one ring can be expressed as a linear combination [18, 23] of the other 7. Similarly, in each tetrahedron, one ring can be expressed as a linear combination of the other 3. Thus, we subtract $4 + 8$ from 32, to get a total of 20 linearly independent rings in each unit cell. Terms proportional to n_L^2 , n_L and the constant come from the boundary effect. Therefore as the number of atoms becomes large, the multiplicities per N converge as is seen in Fig. 2.

In the case of the perfect FCC crystal, the points on the diagonal are due to numerical artifacts, and therefore their multiplicities do not scale as n_L^3 . If a small perturbation such as thermal fluctuation is added to the crystal and resolves the degeneracy, the points with high multiplicities in the PDs will split and distribute with finite width. Then, the distorted octahedral cavities generate the secondary rings and cavities close to the diagonal and yield the high multiplicities scaled to n_L^3 , as will be shown later (See Fig. 5).

The second example is a uniform random configuration scattered in a cubic box. This is a model for the ideal gas. In this case, Q is composed of N points sampled from the uniform random distribution on $[0, L]^3$, and hence the number density of the system

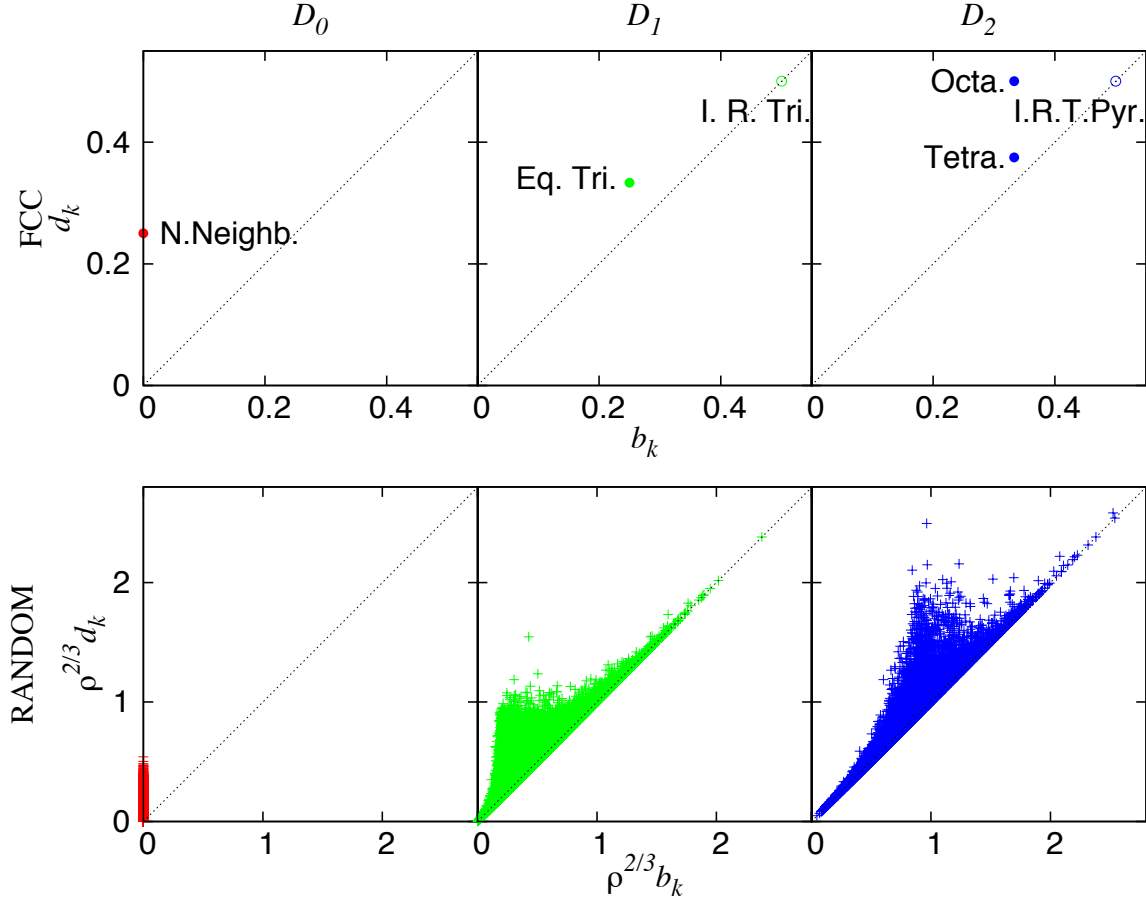


Figure 1. D_0, D_1 and D_2 are shown in the left, center and right panels respectively. The top panels correspond to the cubic cluster of the perfect FCC crystal with $n_L = 10$. The point at $(0, 1/4)$ in D_0 represents the contact to the nearest neighbor atoms, $(1/4, 1/3)$ in D_1 represents equilateral triangle ring, $(1/3, 3/8)$ and $(1/3, 1/2)$ in D_2 represent tetrahedron and octahedron cavities respectively. The bottom panels correspond to a uniform random configuration composed of $N = 27000$ particles scattered in the cubic box $[0, L]^3$. Each point in the PDs for the perfect FCC crystal has high multiplicity, whereas PDs for the uniform random configuration have broad distributions.

is $\rho = N/L^3$. The bottom panels in Fig. 1 correspond to the PDs for the system with $N = 27000$. The PDs show a broad 2-dimensional distribution except for D_0 whose birth scales are zero.

3.1. $\beta_n(\alpha)$: Betti Number

As seen in the two examples, both the broadness of distribution and the multiplicity in the PDs well describe atomic structures of the bulk system. For further study of the multiplicity, we define the Betti numbers $\beta_n(\alpha)$ as

$$\beta_n(\alpha; \mathcal{A}) \equiv \int_{\alpha}^{\infty} dd \int_{\alpha_{\min}}^{\alpha} db \sum_{k \in D_n} \delta(b - b_k) \delta(d - d_k) \quad (2)$$

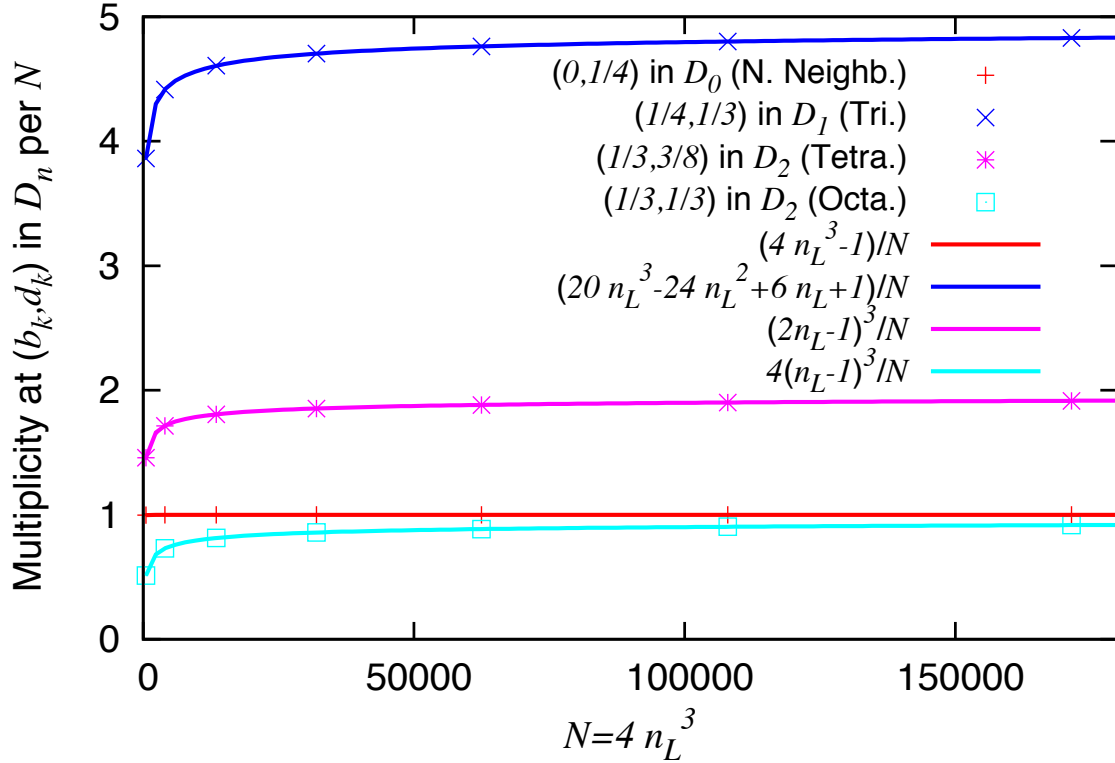


Figure 2. Multiplicities at (b_k, d_k) in D_n per the number of particle N for perfect FCC crystal are plotted as a function of N . These values converge to their bulk values like $m(n)/n^3$, where $m(n)$ is a third-order polynomial.

for a given α . In Fig. 3, $\beta_n(\alpha)$ for $N = 4000, 32000$, and 1715000 with $\rho = \sqrt{2}$ for the FCC crystal (top panel) and $N = 1000, 27000$, and 125000 with $\rho = 1$ for the uniform random configuration (bottom panel) are plotted.

For the crystal, $\beta_n(\alpha)$ is a piecewise constant function, whereas $\beta_n(\alpha)$ for the uniform random configuration is a single peak function. The plateau values of β_n for the FCC crystal are represented by the multiplicities in D_n . Namely, the plateau values of β_0, β_1 , the first and second plateau of β_2 are equal to $m_{\text{N.Neighb.}}, m_{\text{Tri.}}, m_{\text{Tetra.}} + m_{\text{Octa.}}$, and $m_{\text{Octa.}}$ respectively. Therefore, they are proportional to N for the asymptotically large N . It is noteworthy that $\beta_2(\alpha)$ cannot separate the number of tetrahedra and octahedra even though D_2 can. In this sense, PDs have richer information than the Betti numbers.

For a uniform random configuration, the curves of $\beta_n(\alpha)$ seem to be scaled to N as seen in the insets of the bottom panel in Fig. 3. To illustrate the scaling, we compare the peak values $\beta_{n*} \equiv \max_{\alpha} \beta_n(\alpha)$ against N and confirm that the peak values β_{n*} are asymptotically proportional to N (Fig. 4). Therefore, for given α , $\beta_n(\alpha)$ is an extensive variable for the system. However, only in the case $n = 0$ and for large α , this extensively fails because $\beta_0(\alpha) = 1$ and is independent of the system size.

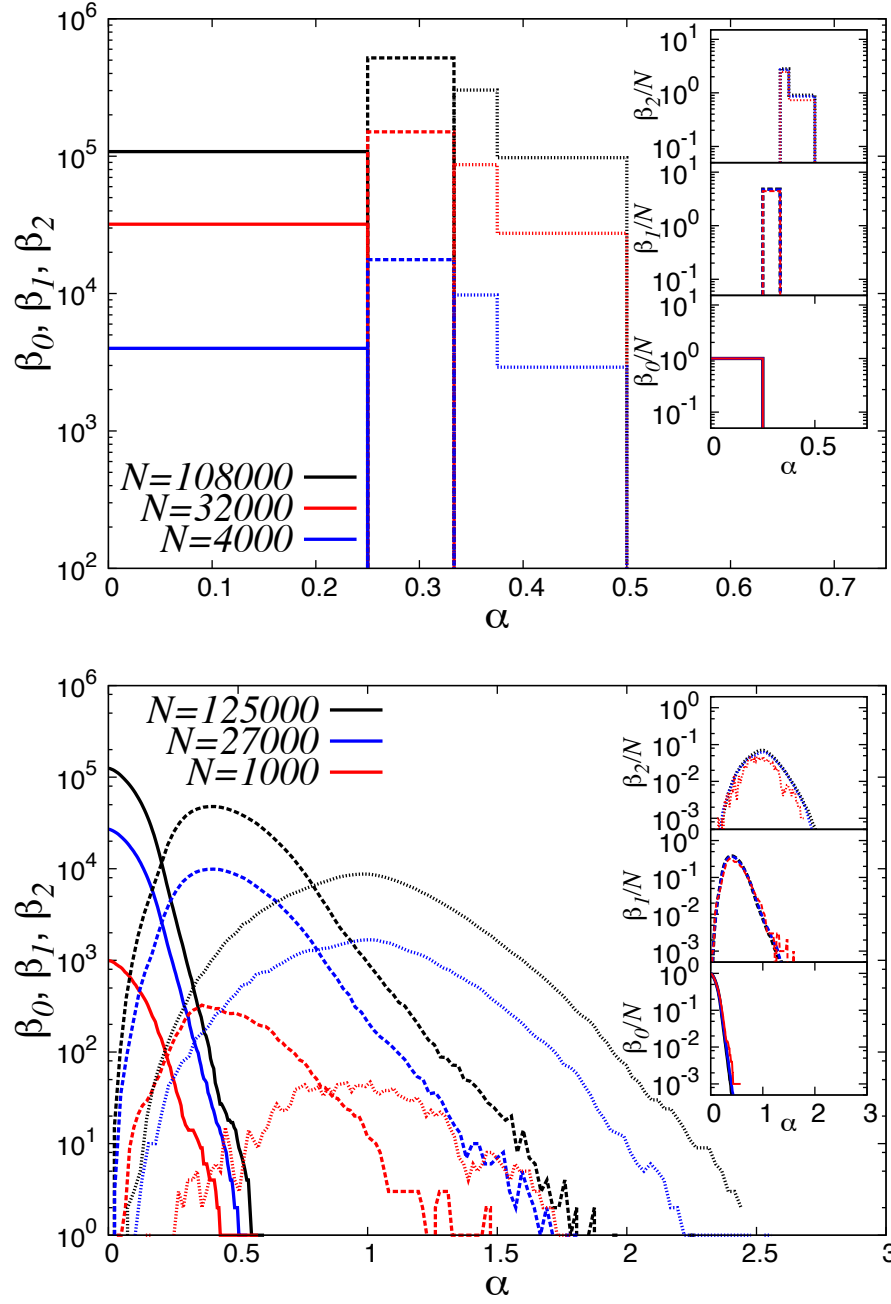


Figure 3. Betti numbers $\beta_n(n = 0, 1, 2)$ are plotted against the variable α for the perfect FCC crystal with number density $\rho = \sqrt{2}$ (top) and the uniform random distribution with fixed number density $\rho = 1$ (bottom) for several N . The solid, dashed, and dots lines correspond to the β_0, β_1 and β_2 respectively. Insets: Betti numbers per N are plotted as functions of α .

3.2. $\xi_n(b, d)$: Normalized Distribution for D_n

Because the Betti numbers are asymptotically proportional to N for the examples above, it is natural to introduce the two-variable normalized distributions for $D_n(\mathcal{A})$

$$\xi_n(b, d; \mathcal{A}) \equiv \frac{\rho^{-4/3}}{N} \sum_{k \in D_n} \delta(b - b_k) \delta(d - d_k) \quad (3)$$

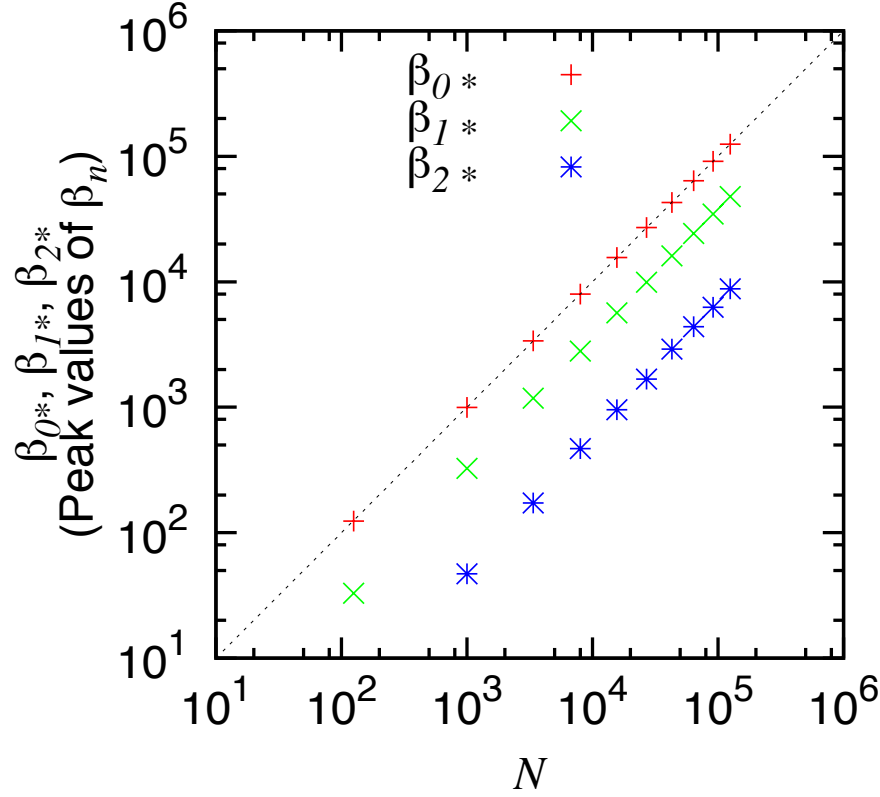


Figure 4. The peak values of $\beta_n(\alpha)$ for the uniform random configuration are plotted against the number of the atoms N . These values are proportional to N in asymptotically large N .

for $n = 1$ and 2 . Here, the factor $\rho^{-4/3}$ is introduced to make ξ_n dimensionless. Because ξ_n is a distribution function whose argument is (b, d) , its horizontal and vertical axes are b and d , different from the scatter plot D_n whose axes are b_k and d_k . In the case of $n = 0$ for the monatomic system with input radius r , every birth scale takes the same value $b_k = -r$. Hence, we define ξ_0 as a function of d by

$$\xi_0(d; \mathcal{A}) \equiv \frac{\rho^{-2/3}}{N} \sum_{k \in D_n} \delta(d - d_k). \quad (4)$$

For the FCC crystal, as was seen in Fig. 2, because the multiplicity for each point asymptotically scales to N , ξ_n converges as N become large. We also validate this convergence for non-zero temperature crystal obtained by MD simulation for Lennard-Jones (LJ) particles' system. The parameters of the potential $u(r) = 4\epsilon((\sigma/r)^{12} - (\sigma/r)^6)$ are set to be $\epsilon = \sigma = 1$. Starting from the perfect crystal configuration, NPT (Nosé-Hoover-Anderson) simulation at temperature $T = 0.1$ and pressure $P = 1$ in LJ unit has been carried out to obtain the equilibrium configuration of the FCC crystal. As a reference, we have also calculated PDs for the perfect crystalline configuration at $T = 0, P = 1$ obtained by energy minimization. According to the top panel of Fig. 5, ξ_n is distributed with non-zero width around the spike corresponding to the perfect crystal.

Similar to the perfect crystal, the distributions for the ξ_1 and ξ_2 surfaces converge asymptotically large N . In the PDs, each geometric object forms one isolated island domain over the diagonal, which is characteristic for the crystalline solid. In addition, peaks close to the diagonal in ξ_1 and ξ_2 also converge asymptotically large N , different from the perfect crystal, therefore they are no more numerical artifact. Both rings and cavities in these regions are generated by the octahedra. This is a typical example, where one primary hole generates other secondary holes. In this case, the octahedral cavity is the primary hole and the rings and cavities close to the diagonal are the secondary holes.

For the uniform random configuration, $\xi_n(\rho^{2/3}b, \rho^{2/3}d)$ is a scaling functions. Intuitively, the birth and death scales become smaller as the number density ρ becomes larger. This effect is cancelled by replacing the arguments of ξ_n by $(\rho^{2/3}b, \rho^{2/3}d)$, as seen in left panels of Fig. 6 for $N = 6400$, $L = 40$ and 10. The left panels in Fig. 6 also show the statistical convergence for $\rho = 1$ with $N = 1000$, 64000, and 125000. For small N , only the points close to the diagonal appear because holes with short life scales are the majority in the random configuration. In contrast, a large N is necessary to detect holes with long life scales. The right panels in Fig. 6 show the scaling function for $N = 125000$. The derivation of this scaling function is explained in Appendix A.

To grasp the meaning of the topological description using (2) and (3), we compare them to the coordination number n_{CN} and the radial distribution function $g(r)$. Recall that n_{CN} and $g(r)$ satisfy the following relation:

$$n_{\text{CN}} = \int_0^{r_c} dr 4\pi r^2 \rho g(r). \quad (5)$$

In Fig. 7, we see that ξ_0 and $1 - \beta_0/N$ show similar behaviors to $g(r)$ and n_{CN} . In fact, β_0 and ξ_0 satisfy

$$\frac{\beta_0(\alpha)}{N} = \rho^{2/3} \int_{\alpha}^{\infty} dd \xi_0(d),$$

and by using $\beta_0(\alpha_{\min}) = N$, we obtain

$$1 - \frac{\beta_0(\alpha)}{N} = \rho^{2/3} \int_{\alpha_{\min}}^{\alpha} dd \xi_0(d). \quad (6)$$

Different from the radial distribution $g(r)$, $\xi_0(d)$ is determined by many-body atomic configurations. Actually, as long as the dimers are counted in the small scale, they yields the same distribution. However, as the scale becomes larger, such as the cluster composed of more than 2 atoms, these distributions deviate each other. For $n = 1, 2$, the relation between ξ_n and β_n is given by

$$\frac{\beta_n(\alpha)}{N} = \rho^{4/3} \int_{\alpha}^{\infty} dd \int_{-\infty}^{\alpha} db \xi_n(b, d). \quad (7)$$

Even though we show the extensivity of Betti numbers β_n and the normalization of ξ_n only for the monatomic system, these properties are expected to be satisfied even for the multi-component system as long as the system is macroscopically uniform.

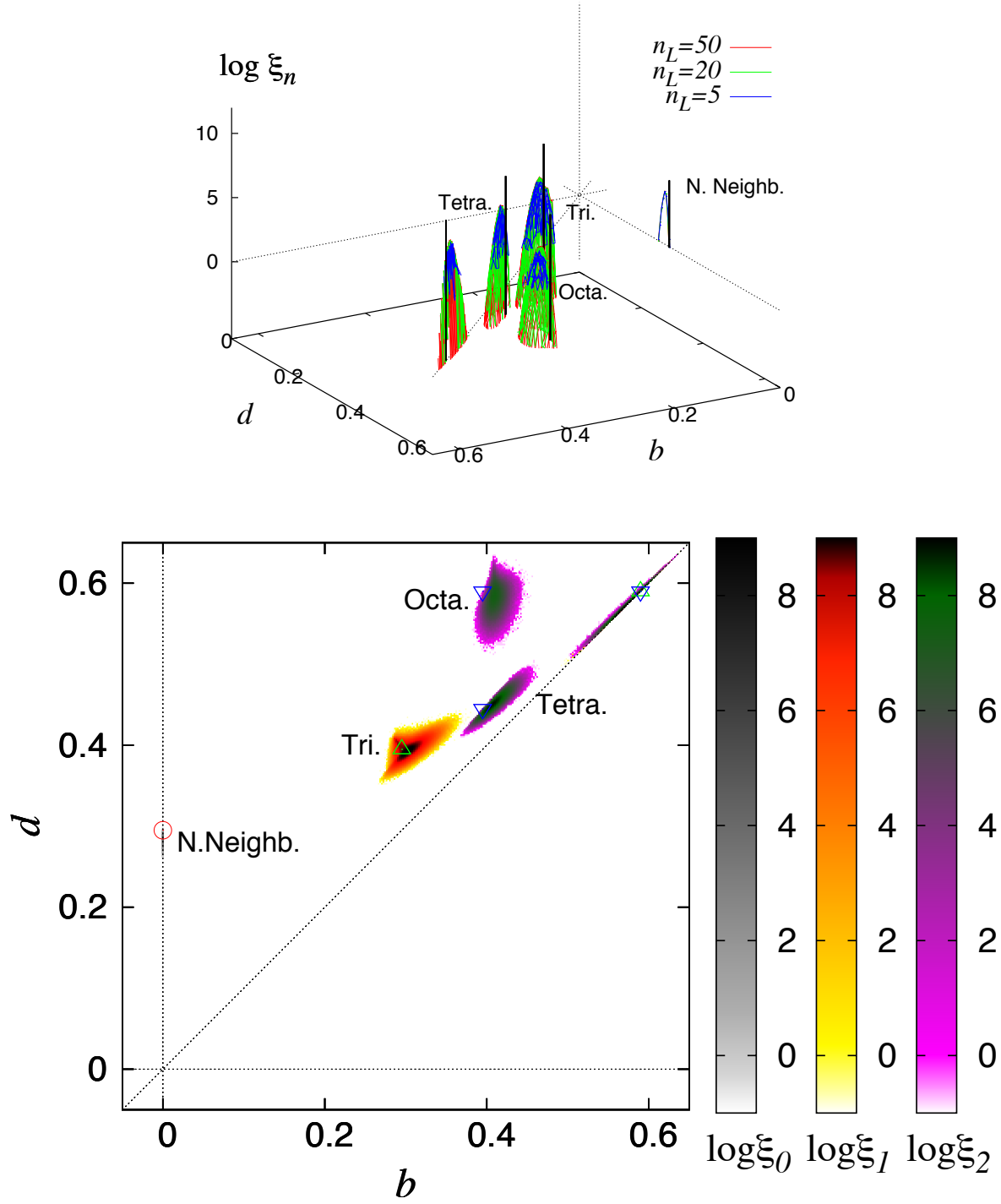


Figure 5. ξ_n for Lennard-Jones FCC crystal of temperature $T = 0.1$ and pressure $P = 1$ in LJ unit. The convergence of ξ_n for $n_L = 50, 20, 5$ (top panel). The contour map of ξ_n for $n_L = 50$ (bottom panel). The spikes in top panel and the circle and triangles in bottom panel correspond to the configuration obtained by energy minimization, and therefore correspond to the configuration of perfect FCC crystal.

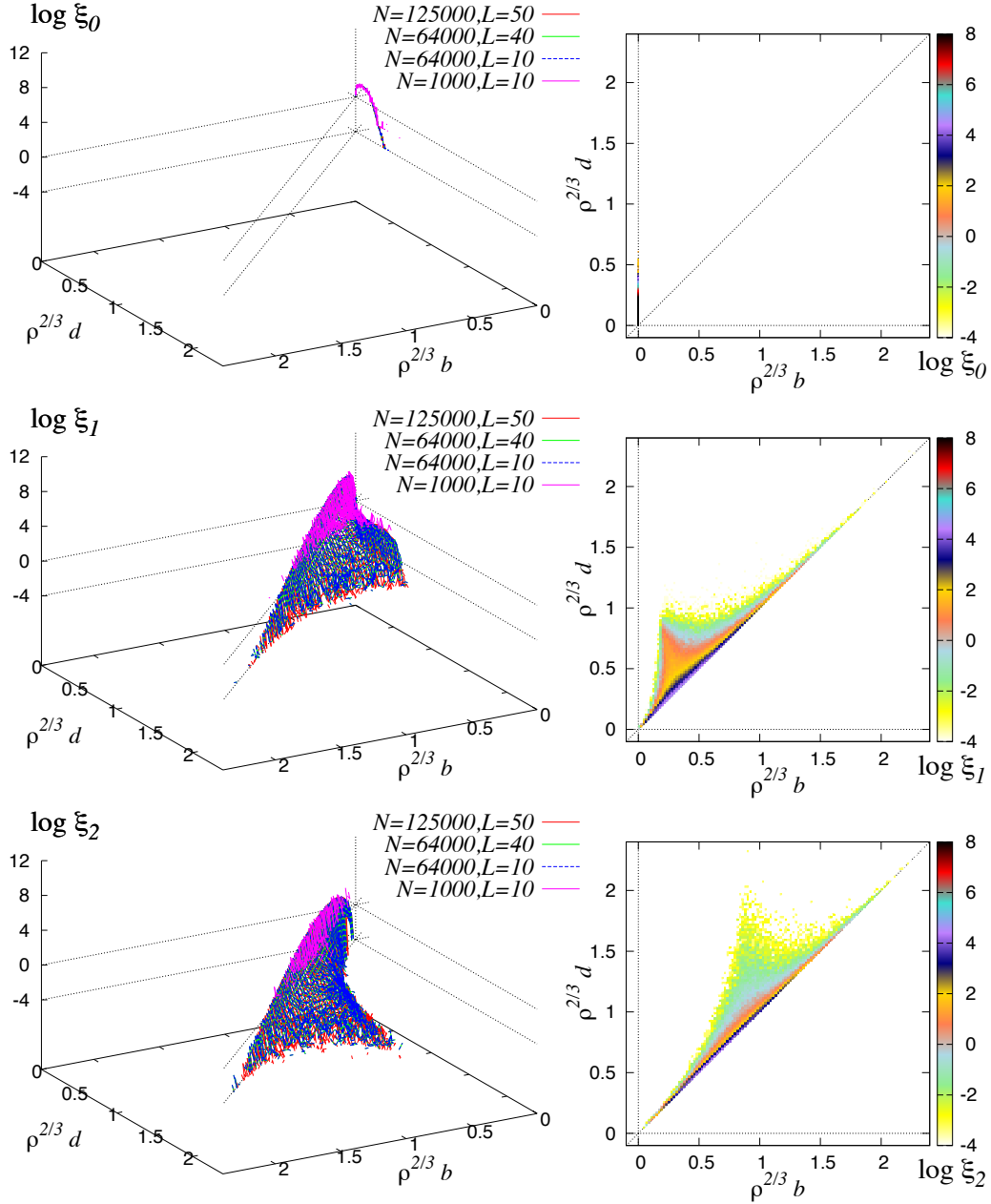


Figure 6. The convergence and collapse of ξ_n for the uniform random configuration (left panels). For fixed number density $\rho = N/L^3 = 1$, the convergence of ξ_n is observed as N becomes larger (red, green and magenta surfaces). For fixed $N = 64000$, ξ_n for $L = 10$ and 40 (green and blue surfaces) collapse as a function of $(\rho^{2/3}b, \rho^{2/3}d)$. The contour maps of ξ_n (right panels) for the uniform random configuration with $N = 125000$, $L = 50$ as a function of $(\rho^{2/3}b, \rho^{2/3}d)$.

4. Multi-Component System: Silica Glass

In this section, we discuss how to apply the PD analysis to multi-component systems, and explain how to get multi-scale geometric information from the PDs. We choose silica

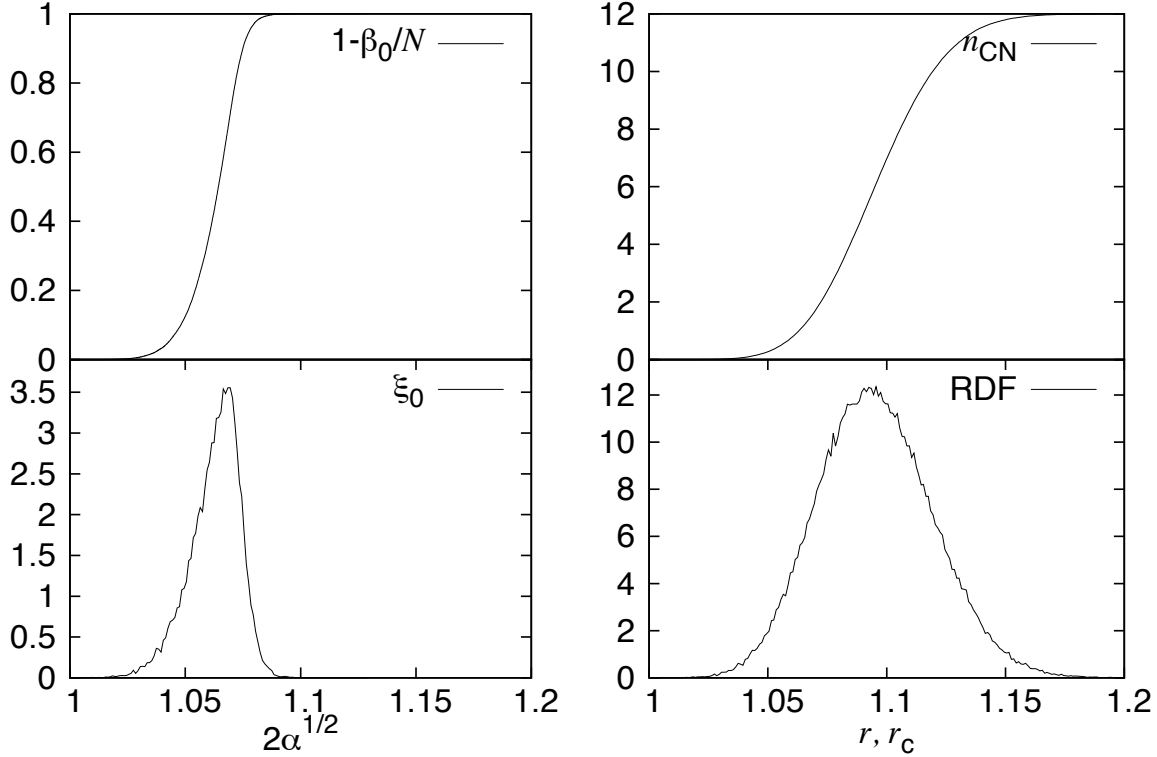


Figure 7. Correspondence of the relation between radial distribution function (right bottom) and coordination number (right top) and between ξ_0 (left bottom) and $1 - \beta_0/N$ (left top) for the FCC crystal of temperature $T = 0.1$ and pressure $P = 1$ in LJ unit. The length scale in ξ_0 and $1 - \beta_0/N$ is rescaled to $2\alpha^{1/2}$, which corresponds to the distance between two atoms in a 2-body distribution.

glasses as examples. The atomic configurations of silica glasses have been obtained by the cooling MD simulation using BKS potentials [27, 25, 26].

4.1. Single-Component Analysis

In a single-component analysis, the input to the PDs is given by the individual configurations of oxygen and silicon atoms extracted from SiO_2 atoms. Fig. 8 shows the PDs of the oxygen and silicon configurations, respectively. Similar to the previous section, we use the uniform input radius $r = 0$ for all atoms by using the invariance under the transformation. As we see later, this invariance property can be used to determine the atomic compositions of the holes in the multi-component analysis.

We observed that both the birth and death scales of the silicon atoms are larger than those of the oxygen atoms. This is because the silicon atoms are distributed more sparsely than the oxygen atoms. Furthermore, we found several characteristic domains in the PDs: straight lines parallel to the death axis (fixed birth scale) in D_1 , a curve departing from the diagonal in D_1 , and a spot domain I_T around $(b, d) = (2.4, 2.6)$ in

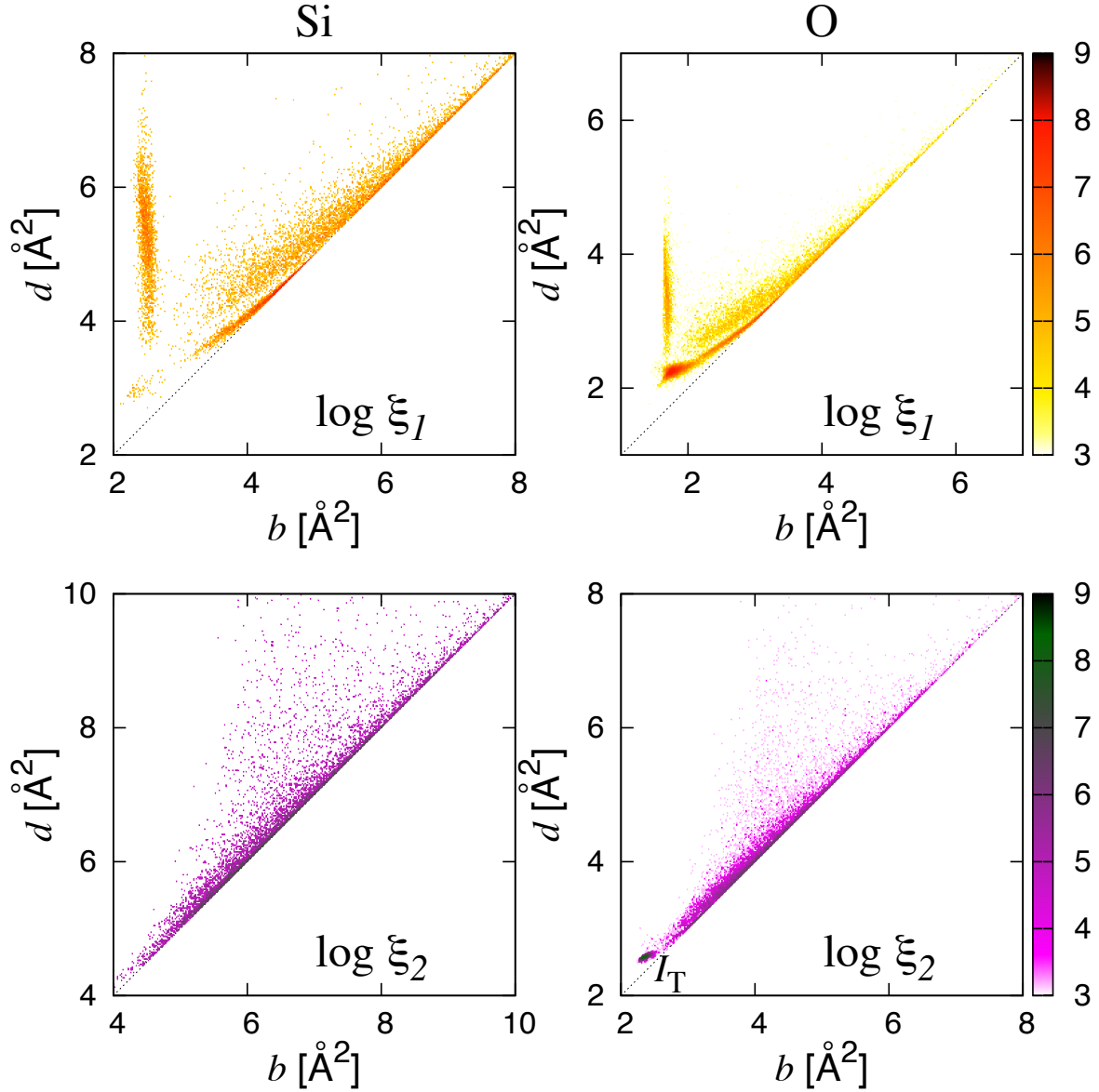


Figure 8. PDs for the silicon (left) and oxygen (right) configurations in the amorphous silica.

D_2 for the oxygen configuration.

Comparing with the PDs for the uniform random distribution, these characteristic domains also encode geometric structures in the single-component configurations. For example, the vertical line determined by the fixed birth scale ($b = b_*$) in D_1 show the existence of a geometric structure in the rings on the line. Recall that from the definition, the birth scale measures the distance to the neighboring atoms in the ring. This means that the rings on the straight line possess the fixed distance $2r(\alpha) = 2\sqrt{b_*}$ to the neighboring atoms. On the other hand, the diversity of the straight line parallel to the death direction means a variety in the sizes of the rings. Moreover, we found that a ring on the curve close to the diagonal in D_1 is generated by the ring on the vertical

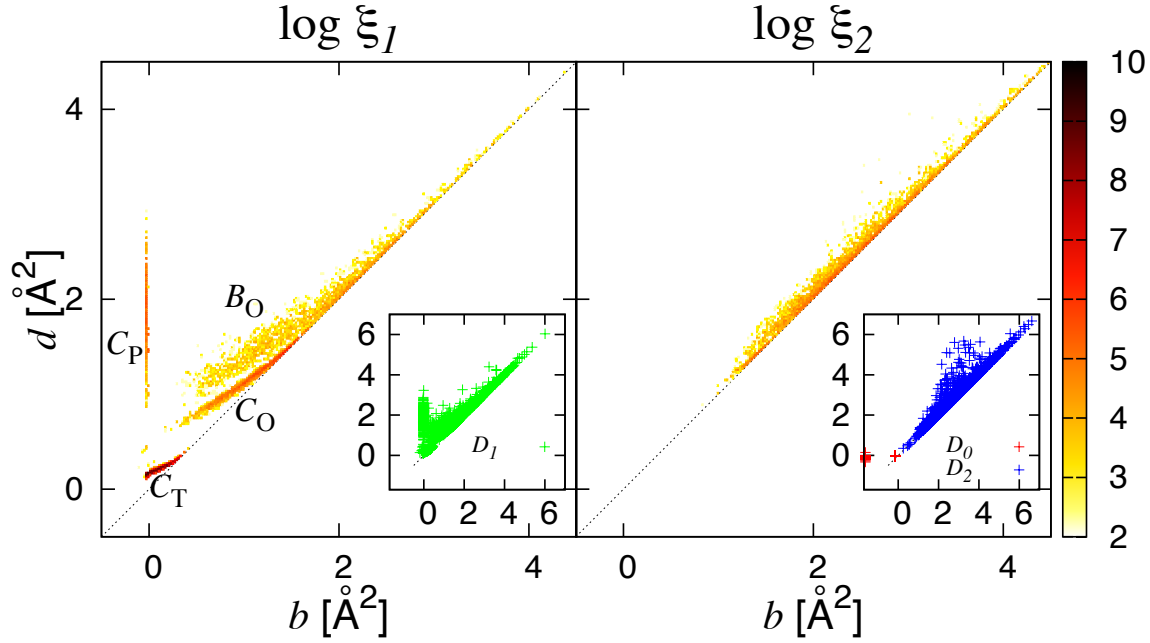


Figure 9. ξ_1 (left panel) and ξ_2 (right panel) for an amorphous silica. D_0 , D_1 and D_2 are described in the inset. The characteristic curves are observed in ξ_1 .

line, which is similar to octahedron in FCC. We can also show that the spot domain I_T represents tetrahedra composed of 4 oxygen atoms each.

4.2. Multi-Component Analysis

4.2.1. Existence of Characteristic Curves Different from the single-component analysis, the PDs in this case depend on the choice of input radii parameter $R = (r_1, r_2, \dots, r_N)$. One of the ways to set R is using partial radial distribution functions of the atomic configuration. Namely, we investigate the first peak positions of pairwise distributions, and set the initial radius for each type of atom by solving linear constraints determined by these peak positions. For example, in the atomic configuration of the amorphous silica, we chose the smallest two peaks $d_{\text{SiO}} = 1.65\text{\AA}$ and $d_{\text{OO}} = 2.55\text{\AA}$ (Si-O and O-O pairs, respectively). Then, solving the two constraints $r_{\text{Si}} + r_{\text{O}} = d_{\text{SiO}}$ and $2r_{\text{O}} = d_{\text{OO}}$, we obtain the input radii $r_{\text{Si}}^* = 0.375\text{\AA}$ and $r_{\text{O}}^* = 1.275\text{\AA}$. Fig. 9 shows the PDs of the amorphous silica for these input radii parameters.

In the previous work [27], the PDs of silica glasses and the hierarchical geometric ring structures are studied in detail. We summarize here some of the results which are relevant to the later discussion in this paper. First of all, three characteristic curves, C_P , C_T and C_O , and one band region B_O are found in D_1 of Fig. 9. The rings on C_P have the property that they generate secondary rings when the rings get pinched as the parameter α increases [27]. Here P is named after *primary* and the mechanism is similar to the octahedron cavity in the FCC. The resulting secondary rings are located on C_T , C_O , and B_O .

We also note that the cavity distribution in D_2 for the amorphous silica shows no characteristic regions. In particular, the spot domain I_T disappears. This is because the silicon atoms are placed in the interior of the 4-oxygen tetrahedra.

From the PDs, we can conclude that the ring structures are more essential than the cavities in the amorphous silica. This is consistent with the fact that existing methods such as ring statistics well characterize the amorphous silica. Hereinafter, we only discuss D_1 .

4.2.2. Classification of Curves By changing the radius parameter R , we can obtain further information such as the composition of the rings. In Fig. 10, several D_1 are shown for the different input radii. The radii are set to be $r_{\text{Si}} = r_{\text{Si}}^* - 0.2\text{\AA}$, r_{Si}^* , $r_{\text{Si}}^* + 0.2\text{\AA}$, and $r_{\text{Si}}^* + 0.4\text{\AA}$ for the silicon, and $r_{\text{O}} = r_{\text{O}}^* - 0.4\text{\AA}$, $r_{\text{O}}^* - 0.2\text{\AA}$, and r_{O}^* for the oxygen.

As the input radius of oxygen becomes larger, the death and birth scale become smaller for fixed input radius of silicon r_{Si}^* (the top left panel in Fig. 10). However, two regions C_{O} and B_{O} overlap for the different choice of r_{Si} after the transformation $(b_k, d_k) \rightarrow (2\sqrt{b_k + r_{\text{O}}^2}, 2\sqrt{d_k + r_{\text{O}}^2})$ (the bottom left panel in Fig. 10). As we discussed in the single-component analysis (see the right panel in Fig. 8.), $(b_k + r_{\text{O}}^2, d_k + r_{\text{O}}^2)$ represents the transformation induced by the input radius r_{O} . Hence, the overlap on the transformed coordinates means that the birth and death scales for the rings on C_{O} and B_{O} are determined by oxygen.

Similarly, we found that C_{P} is invariant to the input radii after the transformation $(b_k, d_k) \rightarrow (\sqrt{b_k + r_{\text{Si}}^2} + \sqrt{b_k + r_{\text{O}}^2}, 2\sqrt{d_k + r_{\text{O}}^2})$ (the center panels in Fig. 10.). This means the birth scale is determined by the length between silicon and oxygen, and death scale is determined by the length between oxygen atoms. For C_{T} , we found the invariance via $(b_k, d_k) \rightarrow (\sqrt{b_k + r_{\text{Si}}^2} + \sqrt{b_k + r_{\text{O}}^2}, \sqrt{b_k + r_{\text{Si}}^2} + \sqrt{d_k + r_{\text{O}}^2})$ (the bottom right panel in Fig. 10), meaning that the both scales are controlled by the silicon and oxygen atoms.

Using this procedure, we can classify the regions with respect to the atoms determining the birth and death scales. Furthermore, we can also investigate the compositions of the rings by finding optimal rings [24]. For example, it can be shown that the rings on C_{O} and B_{O} consist of only oxygen atoms.

4.2.3. Geometric Constraints Encoded in Curves In contrast to the 2-dimensionally broad distribution of the PDs for the random configuration, the curves indicate that there exist geometric relations in the atomic configuration. Concretely, the sharp distribution normal to the curve represents a geometric constraint on the rings, whereas the broad distribution along the tangential direction represents a variety of rings.

As shown in Fig. 9, C_{P} lies parallel to the death axis on a fixed birth scale. It follows from the invariance with respect to the input radii after the transformation that the birth scale is determined by the bond between silicon and oxygen. Thus, we can conclude that the geometric constraint in C_{P} means there is a sharp distribution of the Si-O bond length. On the other hand, the diversity of the arrangements of the rings

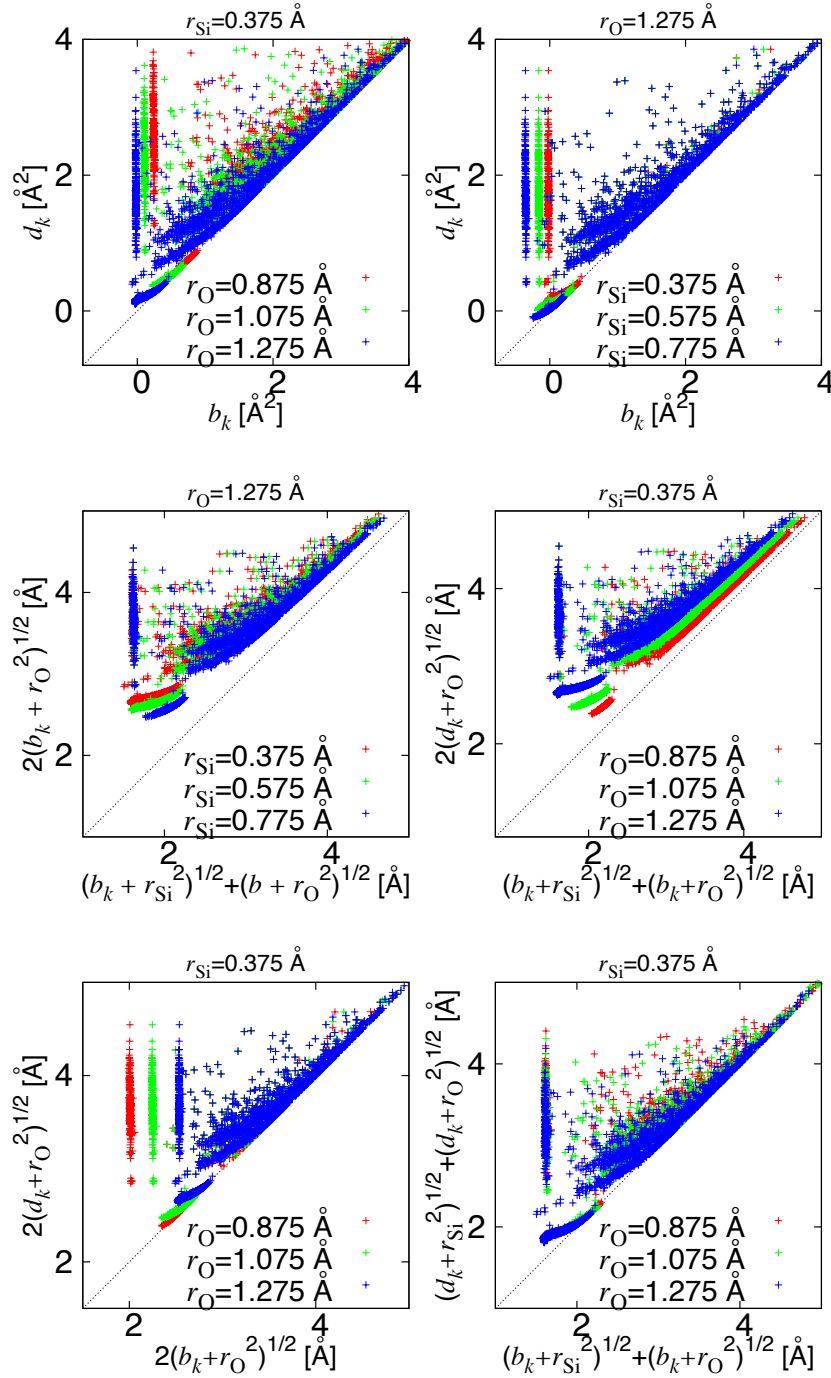


Figure 10. The PDs for several input radii are described. For fixed $r_{\text{Si}} = r_{\text{Si}}^* = 0.375$, $r_{\text{O}} = r_{\text{O}}^* - 0.2\text{\AA}$, r_{O}^* , and $r_{\text{O}}^* + 0.2\text{\AA}$ are described in the top left panel. For fixed $r_{\text{O}} = r_{\text{O}}^* = 1.275$, $r_{\text{Si}} = r_{\text{Si}}^*$, $r_{\text{Si}}^* + 0.2\text{\AA}$ and $r_{\text{Si}}^* + 0.4\text{\AA}$ are described in the top right panel. The overlap of C_P is observed under the transformation $(b_k, d_k) \rightarrow (\sqrt{b_k + r_{\text{Si}}^2} + \sqrt{b_k + r_{\text{O}}^2}, 2\sqrt{d_k + r_{\text{O}}^2})$ in the middle panels. The collapse of C_O and B_O region is observed under the transformation $(b_k, d_k) \rightarrow (2\sqrt{b_k + r_{\text{O}}^2}, 2\sqrt{d_k + r_{\text{O}}^2})$ in the bottom left panel. The collapse of C_T is observed under the transformation $(b_k, d_k) \rightarrow (\sqrt{b_k + r_{\text{Si}}^2} + \sqrt{b_k + r_{\text{O}}^2}, \sqrt{d_k + r_{\text{Si}}^2} + \sqrt{d_k + r_{\text{O}}^2})$ in the bottom right panel.

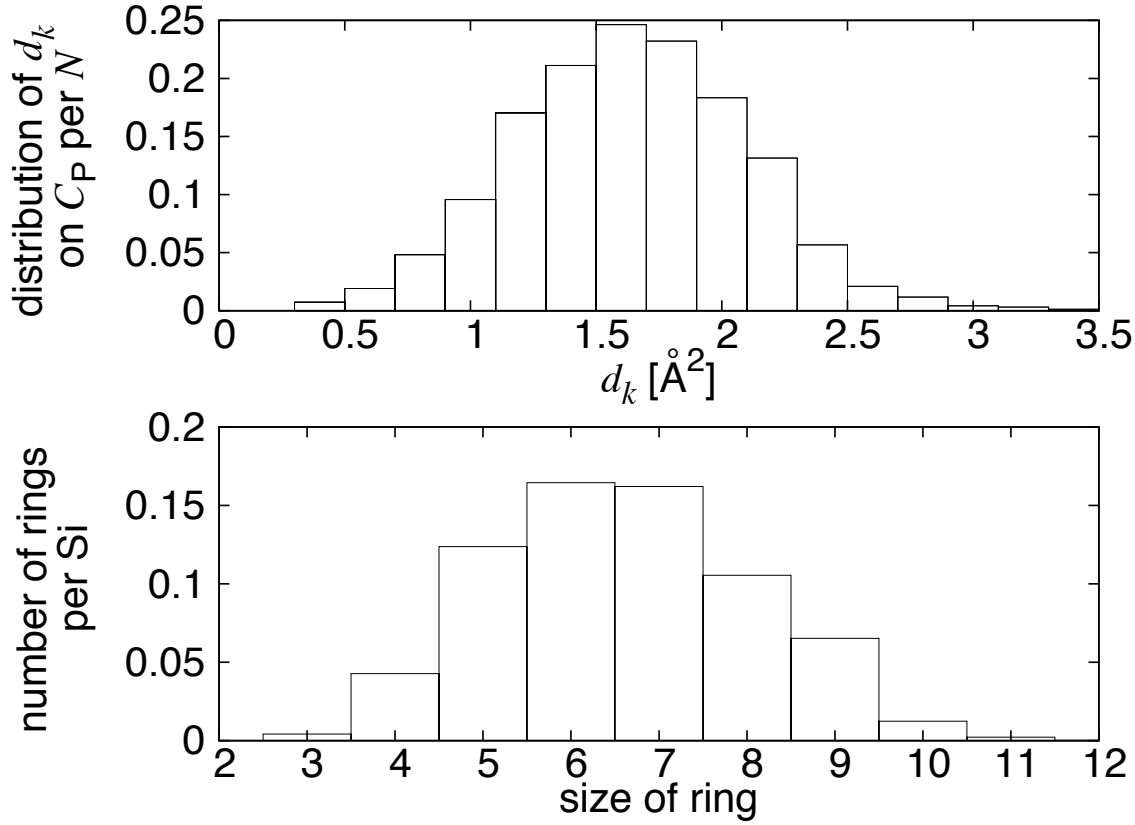


Figure 11. Comparison between the ring statistics (bottom) and the distribution of death scales in C_P (top). Both of them represent the size distribution of the rings constructed by Si-O network.

is mainly controlled by the arrangement of oxygen atoms, and this is represented by the diversity along the death axis. The death scales in C_P describe the size of ring constructed by Si-O network, and hence its diversity corresponds to the ring statistics [1, 8]. Therefore, as is shown in Fig. 11, the ring statistics for the shortest path rings [13] and the death scales in C_P show similar distribution. Even though both of them represent the size distribution of the rings, only the death scale encodes the metric information.

Because the birth and death scales of C_T are controlled by the bond lengths between silicon and oxygen, C_T represents short range order. Fig. 12 shows both C_T and the D_1 for the distorted tetrahedra. Here, the distorted tetrahedra are constructed in such a way that tetrahedra in the local arrangement of SiO_4 require Si-O and O-O bond lengths to be within the first peak of the distributions. Furthermore, their O-Si-O angles and Si-O-O spherical angles are restricted within the 2.5 and 1.5 times the width of the deviation around their mean value, respectively, determined from the configuration obtained by the MD simulation. We found that the curve for the tetrahedron deviates from the C_T if we remove one of the restrictions above. From this observation, the agreement of the two PDs indicates that the geometric structure represented by the

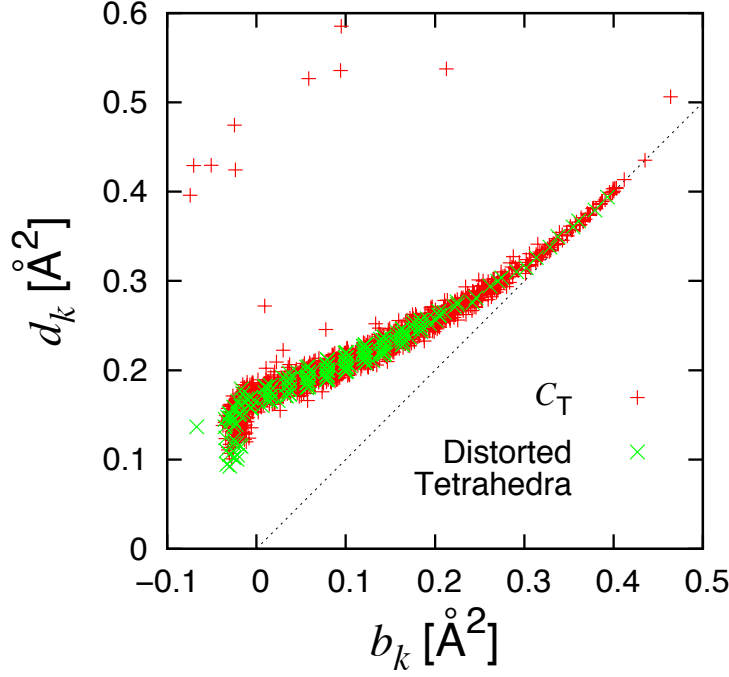


Figure 12. C_T (red) and D_1 for the distorted tetrahedra (green) are described.

curve C_T is a distortion of the SiO_4 tetrahedra.

According to Fig. 9, the birth scales of C_O and B_O are larger than the death scales of C_T . This means that they appear after all triangles in SiO_4 tetrahedra have been covered by the inflated atomic balls. In addition, recall that the rings on C_O and B_O consist of the oxygen atoms in the primary rings at C_P . Thus, they are smaller than C_P , representing the order related to the neighboring of tetrahedra, the so-called Short Range MRO (SRMRO). The geometric constraint corresponding to C_O shows the relationship between O-O length distribution and O-O-O angle distribution. For further details, we refer the reader to the paper [27].

Because PDs can encode many-body atomic structure, we can get a birds-eye view of the geometric hierarchical structure among the various kinds of SRO and MRO. The key point is that a curve in a PD encodes an order in the atomic configuration. Namely, the curve C_T represents SRO, whereas the curves C_P , C_O and B_O show the geometric structure corresponding to MRO in amorphous silica consistent with existing methods.

From the invariance to the input radii, we can convert the death scale d_k of each ring to the real space length $2\sqrt{d_k + r_O^2}$, which shows the diameter of the ring. Since the death scale for the MRO rings (C_P , C_O and B_O) is determined by oxygen, this diameter is independent of the choice of the input radii. The paper [27] shows that this length scale reproduces the typical length scale of MRO corresponding to the first sharp diffraction peak.

5. Concluding Remarks

Persistent homology is a suitable tool to extract many-body atomic structures, and successfully describes geometric features of MRO. The topological approach dramatically reduces the degree of freedom to represent the many-body structures, while keeping metric information and qualitatively important geometric features in MRO.

Several concepts in PD for atomic structures are introduced by choosing two extreme cases: crystalline and random structures. For the crystalline solid, the periodic structure yields a few island supports in ξ_n with high multiplicity, and the diagonal region corresponds to the secondary holes that represent distortion from the primary holes. The shape fluctuation for each hole is represented as a broadness of the peaks in each island. For the random configuration, there are no isolated supports in ξ_n , and a single broad support is found. These observations illustrate the power of PDs to express many-body atomic structures.

As an example of network forming glass materials, ξ_1 for the silica glass shows neither island support nor single broad support but rather characteristic curves that imply the existence of MRO. The primary curve in ξ_1 describes the size distribution of rings, which is similar to the ring statistics. Combining with other curves in ξ_1 , geometric constraint in the MRO is encoded in the PD. With the aid of length scales encoded in PDs, a hierarchical and multi-scale many-body atomic structures are more successfully represented in an integrated manner compared to the existing methods. We believe that this method also has a great potential to describe the other disordered systems, such as complex molecular liquids, packed granular materials, and metallic glasses.

The analysis by the persistent homology is an integrated method incorporating the various existing topological tools. The variables β_0 and ξ_0 are the many-body counterparts of the radial distribution function and the coordination number. The variable ξ_1 in C_P corresponds to the ring statistics. The variable ξ_2 might correspond to the statistics of the Voronoi index, although not mentioned in this paper. Additionally Betti numbers β_n shows extensivity at least for monatomic systems. It is expected that the extensivity is still satisfied for the multi-component system. By using this behavior, the phase transition between macroscopically isotropic phases such as liquid-liquid transition might hopefully be more clearly categorized in the phase diagram.

Appendix A. The Scaling of ξ_n for Uniform Random Configurations

Suppose that N points are sampled from the uniform random distribution in the D -dimensional box $[0, L]^D$. Let the N -point configuration be denoted as $Q_{\text{rnd}}^{N,L} = (\vec{x}_1, \vec{x}_2, \dots, \vec{x}_N)$. Here \vec{x}_i is a D -dimensional position, and N is sufficiently large. Then, the distribution of the n -th persistence diagram $D_n(Q_{\text{rnd}}^{N,L})$ is given as

$$\Xi_n(b, d; Q_{\text{rnd}}^{N,L}) \equiv \sum_k \delta(b - b_k) \delta(d - d_k). \quad (\text{A.1})$$

Here, the (b_k, d_k) are determined by the PD of the union of balls whose radius is $r_i(\alpha) = \sqrt{\alpha}$. The control parameter in the system is the number density $\rho = N/L^D$.

Set m an integer with $m \geq 2$. Because of uniform configuration, $Q_{\text{rnd}}^{mN, \sqrt[m]{m}L}$ shows “similar” behavior as m samples of $Q_{\text{rnd}}^{N,L}$ for sufficiently large N , where we can neglect any boundary effect. Therefore, the distribution Ξ_n is simply multiplied by m

$$\Xi_n \left(b, d; Q_{\text{rnd}}^{mN, \sqrt[m]{m}L} \right) = m \Xi_n \left(b, d; Q_{\text{rnd}}^{N,L} \right) + o(m). \quad (\text{A.2})$$

We expect that Eq. (A.2) be satisfied even when m is real number. The scaling in Eq. (A.2) leads to

$$\Xi_n \left(b, d; Q_{\text{rnd}}^{N,L} \right) = N \tilde{f}(b, d) + o(N). \quad (\text{A.3})$$

Here $\tilde{f}(b, d)$ is the mean value of Ξ_n/N with respect to the uniform random distribution and is independent of N and L , for the sufficiently large N due to the central limit theorem.

In particular, for the uniform random configuration, the birth and death scales change as $(b_k, d_k) \rightarrow (\alpha^2 b_k, \alpha^2 d_k)$ under the transformation, $Q_{\text{rnd}}^{N,L} \rightarrow \alpha Q_{\text{rnd}}^{N,L} \equiv (\alpha \vec{x}_1, \alpha \vec{x}_2, \dots, \alpha \vec{x}_N)$. In addition, $\alpha Q_{\text{rnd}}^{N,L}$ is identical to $Q_{\text{rnd}}^{N, \alpha L}$. Therefore

$$\Xi_n \left(b, d; Q_{\text{rnd}}^{N, \alpha L} \right) = \frac{1}{\alpha^4} \Xi_n \left(\frac{b}{\alpha^2}, \frac{d}{\alpha^2}; Q_{\text{rnd}}^{N,L} \right). \quad (\text{A.4})$$

By using Eqs. (A.2) and (A.4), we obtain

$$\Xi_n \left(b, d; Q_{\text{rnd}}^{N,L} \right) = \frac{v^4}{u^{1+4/D}} \Xi_n \left(\frac{b}{(\sqrt[D]{u}/v)^2}, \frac{d}{(\sqrt[D]{u}/v)^2}; Q_{\text{rnd}}^{uN, vL} \right), \quad (\text{A.5})$$

for the arbitrary u, v . Then, by setting $u = 1/N$, $v = 1/L$,

$$\Xi_n \left(b, d; Q_{\text{rnd}}^{N,L} \right) = N \rho^{4/D} \Xi_n \left(\rho^{2/D} b, \rho^{2/D} d; Q_{\text{rnd}}^{1,1} \right) + o(N) \quad (\text{A.6})$$

is obtained. Here, the argument $Q_{\text{rnd}}^{1,1}$ is formal notation. It should be rewritten by using Eq. (A.2) as

$$\Xi_n \left(b, d; Q_{\text{rnd}}^{N,L} \right) = N \rho^{4/D} f \left(\rho^{2/D} b, \rho^{2/D} d \right) + o(N), \quad (\text{A.7})$$

where $\tilde{f} = \rho^{4/D} f$ and f is dimensionless function. The bottom panels in Fig. 6 shows the collapse of $f(\rho^{2/D} b, \rho^{2/D} d)$ for $D = 3$.

- [1] R. Zallen, *The Physics of Amorphous Solids* (John Wiley & Sons 1983)
- [2] D. E. Polk, J. Non-Crystalline Solids **5**, 365 (1971).
- [3] J. Bernal, Proc. R. Soc. A **280**, 299 (1964).
- [4] Proc. Roy. Soc. Lond. A. **319**, 479 (1970).
- [5] S. Susman, K. J. Volin, D. L. Price, M. Grimsditch, J. P. Rino, R. K. Kalia, P. Vashishta, G. Gwanmesia, Y. Wang, and R. C. Liebermann, Phys. Rev. B **43**, 1194 (1991).
- [6] S. R. Elliott, Phys. Rev. Lett. **67**, 1477 (1991).
- [7] G. N. Greaves and S. Sen, Adv. Phys. **56**, 1 (2007).
- [8] S. R. Elliott, *Physics of Amorphous Material* (Longman. 1990), 2nd ed.
- [9] S. V. King, Nature **213**, 1112 (1967).
- [10] L. Guttman, J. Non-Cryst. Solids **116**, 145 (1990).

- [11] C. S. Mariani and L. W. Hobbs, J. Non-Cryst. Solids **124**, 242 (1990).
- [12] L. W. Hobbs, C. E. Jesurum, V. Pulim, and B. Berger, Philos. Mag. A **78**, 679 (1998).
- [13] D. S. Franzblau, Phys. Rev. B **44**, 4925 (1991).
- [14] K. Goetzke and H. J. Klein, J. Non-Cryst. Solids **127**, 215 (1991).
- [15] X. Yuan and A. N. Cormack, Comput. Mater. Sci **24**, 343 (2002).
- [16] F. Wooten, Acta Cryst. A **58**, 346 (2002).
- [17] W. H. Zachariasen, J. Am. Chem. Soc. **54**, 3841 (1932).
- [18] H. Edelsbrunner and J. Harer, *Computational Topology: An Introduction* (Amer. Math. Soc. 2010).
- [19] G. Carlsson, Bull. Amer. Math. Soc. **46**, 255 (2009).
- [20] Perseus webpage: <http://www.math.rutgers.edu/~vidit/perseus.html>
- [21] PHAT webpage: <https://code.google.com/p/phat>
- [22] CGAL webpage: <https://www.cgal.org>
- [23] A. Hatcher, *Algebraic Topology* (Cambridge University Press. 2001).
- [24] T. Dey *et al.*, SIAM Journal on Computing **40**, 1026 (2011)
- [25] B. W. H. van Beest, G. J. Kramer, and R. A. van Santen, Phys. Rev. Lett. **64**, 1955 (1991).
- [26] K. Vollmayr, W. Kob, and K. Binder, Phys. Rev. B **54**, 15808 (1996).
- [27] T. Nakamura, Y. Hiraoka *et al.*, <http://arxiv.org/abs/1501.03611>